Thermoelectric Transport of Semiconductor Full-Heusler VFe$_2$Al

Journal:	*Journal of Materials Chemistry C*
Manuscript ID	TC-COM-06-2020-002659
Article Type:	Communication
Date Submitted by the Author:	04-Jun-2020
Complete List of Authors:	Anand, Shashwat; Northwestern University, Materials Science and Engineering Gurunathan, Ramya; Northwestern University, Materials Science and Engineering Soldi, Thomas; Northwestern University, Materials Science and Engineering Borgsmiller, Leah; Northwestern University, Materials Science and Engineering Orenstein, Rachel; Northwestern University Department of Materials Science and Engineering Snyder, G.; Northwestern University, Materials Science

SCHOLARONE™
Manuscripts

Thermoelectric Transport of Semiconductor Full-Heusler VFe$_2$Al

Shashwat Anand[1], Ramya Gurunathan[1], Thomas Soldi[1], Leah Borgsmiller[1], Rachel Orenstein[1], and G. Jeffrey Snyder[1]

[1]Materials Science and Engineering, Northwestern University, Evanston, IL, 60208, USA

*jeff.snyder@northwestern.edu

Abstract

The full-Heusler VFe$_2$Al has emerged as an important thermoelectric material in its thin film and bulk phases. VFe$_2$Al is attractive for use as a thermoelectric materials because of it contains only low-cost, non-toxic and earth abundant elements. While VFe$_2$Al has often been described as a semimetal, here we show the electronic and thermal properties of VFe$_2$Al can be explained by considering VFe$_2$Al as a valence precise semiconductor like many other thermoelectric materials but with a very small band gap (E_g = 0.03 +/- 0.01 eV). Using a two-band model for electrical transport and point-defect scattering model for thermal transport we analyze the thermoelectric properties

of bulk full-Heusler VFe$_2$Al. We demonstrate that a semiconductor transport model can explain the compilation of data from a variety of n and p-type VFe$_2$Al compositions assuming a small band-gap between 0.02 eV and 0.04 eV . In this small E_g semiconductor understanding, the model suggests that nominally undoped VFe$_2$Al samples appear metallic because of intrinsic defects of the order of $\sim 10^{20}$ defects/cm^{-3}. We rationalize the observed trends in weighted mobilities (μ_w) with dopant atoms from a molecular orbital understanding of the electronic structure. We use a phonon–point-defect scattering model to understand the dopant-concentration (and, therefore, the carrier-concentration) dependence of thermal conductivity. The electrical and thermal models developed allow us to predict the zT versus carrier concentration curve for this material, which maps well to reported experimental investigations.

Additional Keywords: Thermoelectrics,Fe$_2$VAl, VFe$_2$Al, Heuslers, COHP

1   Introduction

Heusler compounds are cubic structures with the general formula AMM'X where each element, typically all metals, makes a face-centered-cubic sublattice[1]. M and M' are often the same element as in VFe$_2$Al. The resultant compound is usually metallic and considered an intermetallic compound.

There are also many half-Heusler compounds, with general composition AMX where M' is vacant. Many half-Heusler compounds have been shown to be good thermoelectric semiconductors[2,3] where the semiconducting compositions are valence precise so that stable compositions and doping can be predicted using valence counting principles[4,5]. These materials exhibit extraordinary electrical properties[6] and thermal properties which can

be engineered substantially through control of defects[7–10]. The thermoelectric figure of merit (zT) of both n-[11,12] and p-type[13–15] half-Heusler materials are comparable to that of state-of-the-art thermoelectrics. Additionally, these materials have superior mechanical properties[16,17] in comparison to well-known chalcogenide-based thermoelectrics, making them more advantageous for device applications.

The thermoelectric properties of the full-Heusler alloy composition of VFe_2Al has been studied extensively[18] because it is based on non-toxic, inexpensive and earth abundant elements, making it ideal for mass-produced, consumer products for waste heat recovery or refrigeration if sufficient thermoelectric efficiency can be achieved. The thermoelectric power factor of n-type bulk VFe_2Al[18,19] exceeds that of commercially available n-type Bi_2Te_3[20] at room temperature. Recently, remarkable thermoelectric properties were reported in films having the full-Heusler alloy composition of VFe_2Al, but with a metastable body centered cubic structure.[21] Both the high thermoelectric power factor and low thermal conductivity reported in the films[21] warrant a close comparison to the thermal and electrical transport of the full-Heusler bulk material and a better understanding of how its electronic structure leads to its thermal and electrical properties.

Many full-Heusler compounds such as VFe_2Al appear to be stable with 24 valence electrons[1] per formula, which suggests there may be a molecular orbital explanation for the electronic structure and stability near a semiconducting composition as commonly found in Zintl phases[22] and half-Heusler thermoelectrics[23]. Nevertheless, in a majority of studies VFe_2Al has been interpreted as an indirect semimetal (see Figure 1) with a pseudo-gap,[1,18,24,25] due to early photoemission[26], NMR[27] and computational[28–30] studies describing it as a semimetal.

However, some properties of VFe$_2$Al are more consistent with a semiconductor (see Figure 1) rather than a semimetal description[31]. For example, the nominally stoichiometric compound shows a decreasing electrical resistivity with increasing temperature, which is consistent with a semiconductor description[26]. The discrepancy between observed transport and semimetallic understanding of VFe$_2$Al has occasionally been rationalized using possible exotic phenomena such as 3d heavy fermion behavior[26,30]. However, subsequent heat capacity measurements do not appear to corroborate this behavior[32]. As a result, there is no general consensus on the band-gap and the observed transport properties in bulk VFe$_2$Al is poorly understood.
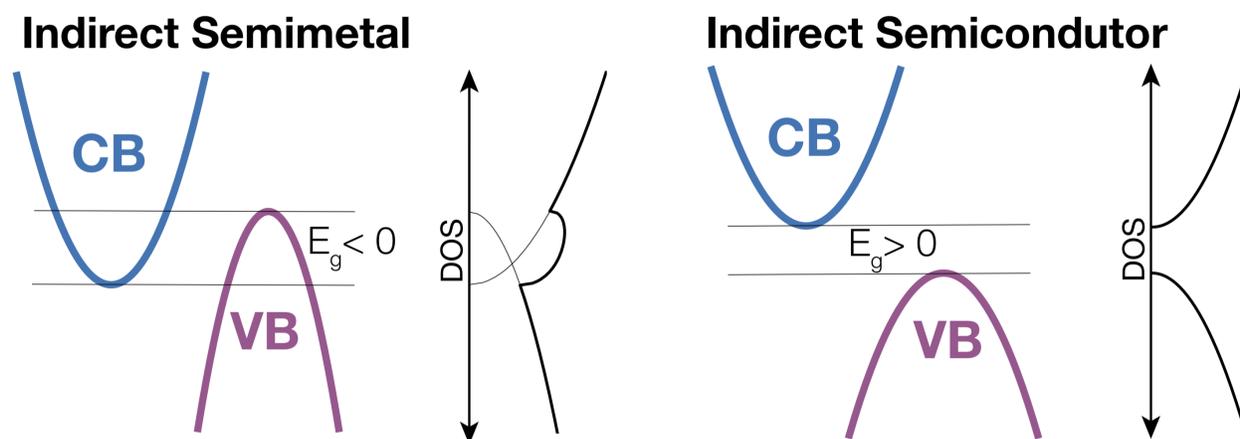
Figure 1 Schematic demonstrating difference between electronic structure of indirect semimetals and semiconductors.

Here we review the thermoelectric properties of a variety of n and p-type VFe$_2$Al samples presented in the literature. We show that the experimental Seebeck coefficient, electrical resistivity and thermal conductivity as a function of temperature and doping is consistent with an interpretation of VFe$_2$Al as a small band-gap semiconductor with $E_g \approx 0.03 \pm 0.01$ eV rather than a semimetal. We attribute the past semimetalic interpretation of experimental data to the large concentration of intrinsic defects in the material

which are present even in undoped VFe$_2$Al. This interpretation enables a modeling of the thermoelectric performance, including a prediction of maximum zT as well as engineering strategies for improving the thermoelectric properties that should be applicable to both bulk and thin film materials.

2 Results and Discussion

2.1 Electronic Structure

Depending on the level of theory used in the first-principles calculations, both semimetallic and semiconducting electronic structures have been reported[28–30,33–39] for VFe$_2$Al in the full-Heusler structure. In calculations showing the semimetallic bandstructure of VFe$_2$Al the hole and electron pockets lie in seperate high symmetry points (namely Γ and X respectively). The valence bands at Γ and the conduction band at X do not overlap in k-space but have the same energy over a 0.1 eV energy range so that the electronic structure can be described as a simple semimetal with negative band gap, $E_g \sim -0.1$eV. In the case of semiconductor band structure reports, the bands look essentially the same with true valence bands at Γ and a conduction band at X but with predicted indirect band-gap (E_g) values > 0.2 eV. Occasionally, the E_g values have been rationalized[33] using experimentally reported 'pseudogap'[24,27] in the electronic structure. However, in these experimental works a semimetallic electronic structure was still expected for VFe$_2$Al and the 'pseudogaps' were not representative of the indirect gap between X and Γ pockets.[24,27]

We calculate the electronic band structure of VFe$_2$Al using GGA+U calculations where the Hubbard U is selected to give a small band-gap E$_g$ = 0.03 eV. We will show in the fol-
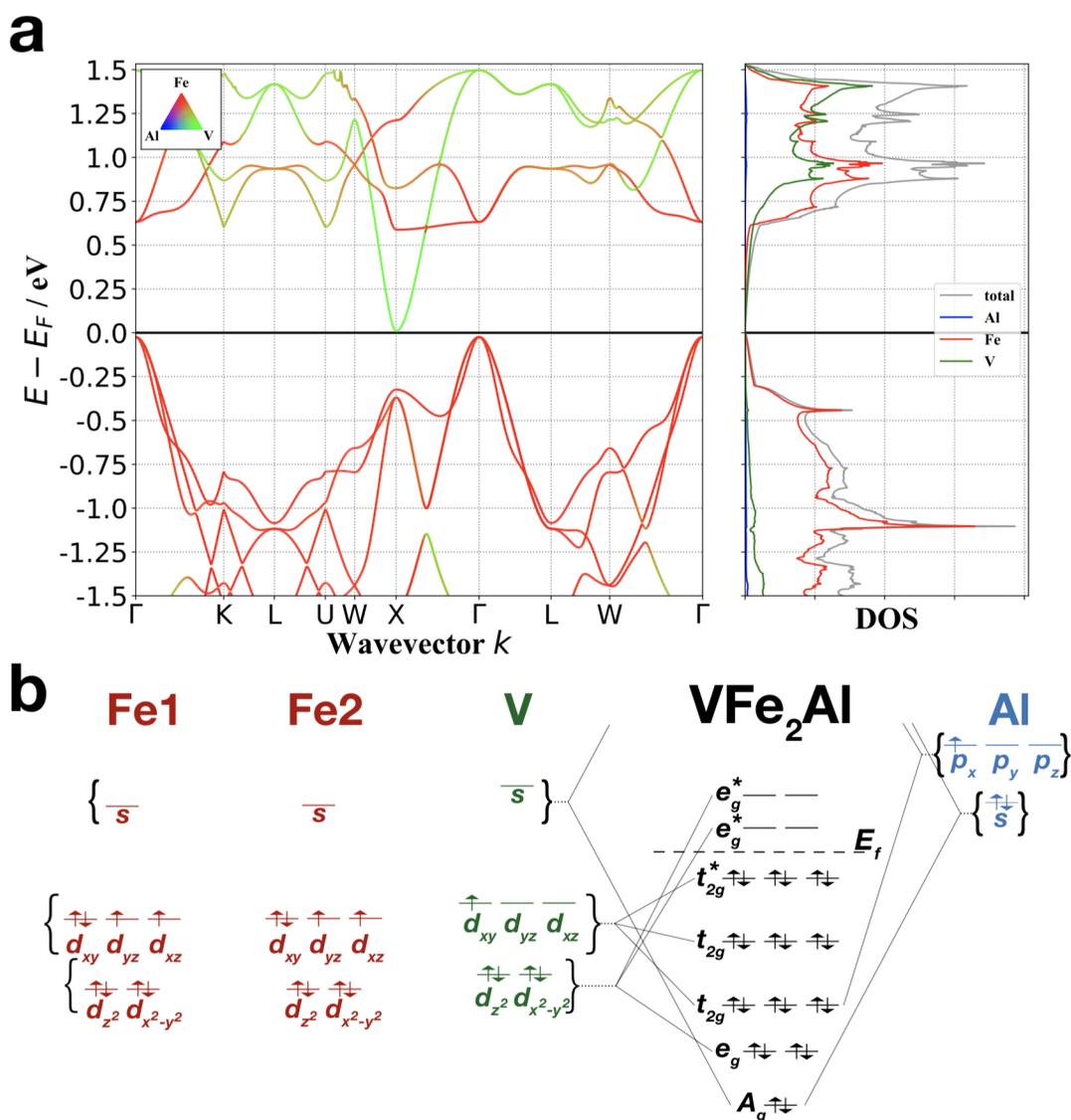
Figure 2 (a) Atom resolved electronic band structure and density of states for VFe$_2$Al. (b) Schematic illustration of the molecular orbital diagram in VFe$_2$Al. The bonding (example e_g) and anti-bonding (example e_g*) interactions are concluded from partial density of states and k-resolved Crystal Orbital Hamilton Population (COHP) analysis of states at the Γ point in the electronic structure (see Figure S1-Figure S15). States close to the Fermi-level (E_f) predominantly show e_g and t_{2g} charater from V and Fe atoms.

lowing sections that this small gap, rather than semimetallic $E_g \sim$ -0.1 eV or the larger gap

of $E_g > 0.1$ eV, is most consistent with the experimentally observed transport properties.

The valence band maximum (VBM) is triply degenerate at the Γ point with a significant Fe

character. The conduction band minimum (CBM), on the other hand, consists of a single

band with V character at X due to highly dispersive V states. The valence and conduction bands have the same valley degeneracy of $N_v = 3$, since the single X-point pocket consists of 6 half-pockets in the Brillouin zone of this cubic structure.

The nature of the electronic bands can be rationalized using molecular orbital (MO) diagrams, which enables insight into the local bonding[23] and its effect on the valence and conduction bands in VFe$_2$Al. To construct the MO diagram (see Figure 2b), we first determine the orbital character of all states at the Γ point using orbital projected partial density of states (pDOS) (see Figure 3). Subsequently, we perform and a k-resolved Crystal Orbital Hamiltonian Population (COHP) analysis to investigate the nature[40] (bonding versus antibonding) and strength of interaction between these orbitals. In our analysis, we consider 4 conduction band states and 12 valence band states each with an occupancy of 2. The valence bands chosen in our analysis contain all the 24 valence electron of the compound (8×2 from Fe, 5 from V and 3 from Al).

We find that, with the exception of the lowest valence band A_g, the valence band states and lowest conduction band states primarily arise from interactions between Fe and V d-states (see Figure 3). Since, both Fe and V are surrounded by a tetrahedral environment, their d-orbitals split into t_{2g} (d_{xy},d_{yz} and d_{zx}) and e_g (d_{z^2} and $d_{x^2-y^2}$) orbitals. The three sets of t_{2g} from V and the two Fe atoms interact to form three filled sets of t_{2g} molecular orbitals in the valence band. The three sets of e_g orbitals interact more strongly than the t_{2g} orbitals pushing two sets above the Fermi-level and only one set lower in the valence band. The relative interaction strength of t_{2g} and e_g orbitals can be seen from their magnitude of COHP values for the conduction and valence band states at the Γ point (see Figure 2b and 3). Generally, the COHP values for e_g interactions are considerably larger than those
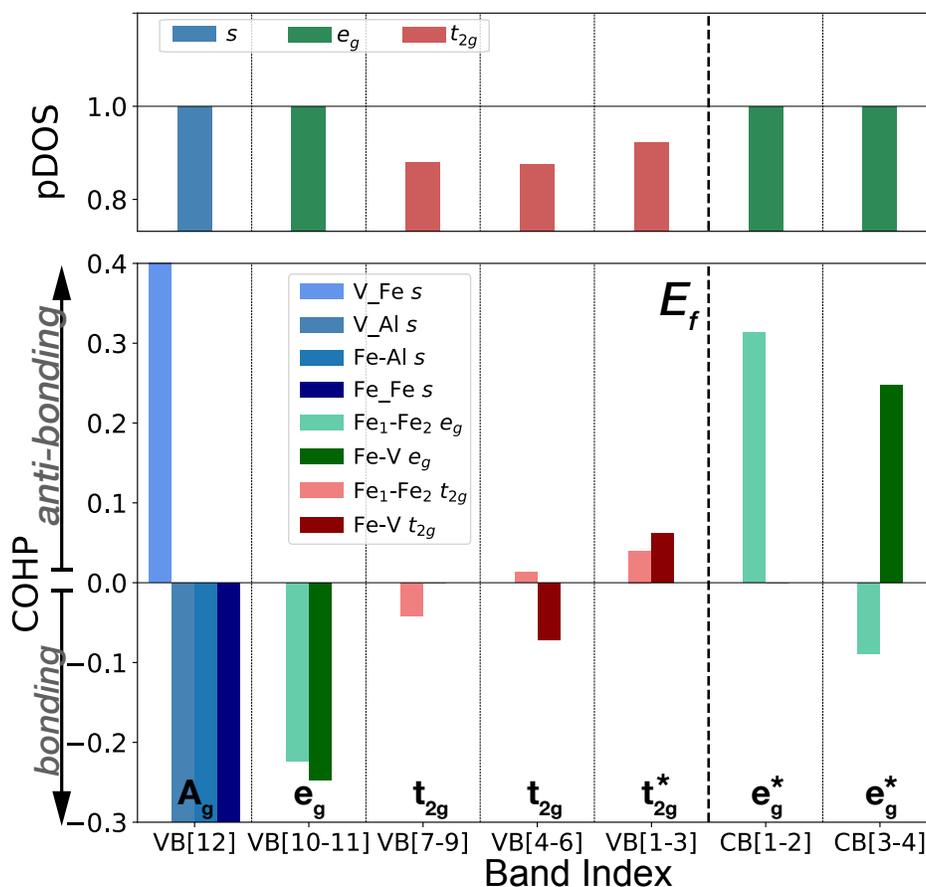
Figure 3 Orbital projected partial Density of States (pDOS) and k-resolved Crystal Orbital Hamiltonian Population (COHP) of Γ-point states of VFe$_2$Al. The x-axis indicates the band index of the Γ-point state. The indices of the valence (VB) and conduction bands (CB) are counted with respect to the Fermi-level (E_f). Degenerate bands are indexed together. The pDOS are determined by adding contributions from s (blue bar), t_{2g}-type (d_{xy}, d_{yz}, d_{zx} red bars) and e_g-type ($d_{x^2-y^2}$, d_{z^2}, red bars) orbitals separately regardless of the atom type. pDOS value of 1 would mean complete contribution from a particular set. The COHP values were determined by averaging across all inter-atomic interactions between orbitals of the same type (for example averaging between Fe d_{z^2} - V d_{z^2} and Fe $d_{x^2-y^2}$ - V $d_{x^2-y^2}$ COHP to obtain Fe-V e_g COHP). Negative and positive COHP values indicate bonding and anti-bonding interactions respectively. COHP value of zero indicates the absence of any interaction. In general, interaction strength increases as $t_{2g} < e_g < s$.

due to t_{2g} interactions. The lowest valence band A_g in the molecular orbital diagram has

a predominantly bonding s-orbital type character with almost equal contributions from all

atoms in the compound (see Figure S14 and Figure 3). The COHP of the A_g largely reveals

a very strong bonding interaction between the s-orbitals, indicating that it originates from

interactions between high energy s-orbitals of the compound (see Figure 3 and 2b).

In general, Al contribution to the valence band states is rather small. While the A_g and the lowest t_{2g} molecular orbitals show some Al contributions (see Figure S14 and Figure S10), the content of Al s and p-states are less than 25% and $\sim$5%, respectively. Among the three elements, Al is the most electropositive (Pauling electronegativity of 1.61) and the small Al content in the the valence bands indicates that the Al can be treated as a Al^{3+} cation within a valence balanced description[5] of this semiconductor compound. With Fe as the most electronegative element, we assign the A_g states and the filled e_g states to Fe giving each 9 electrons or a valence of Fe^{-1}. V, on the other hand, only has its t_{2g} states filled totaling 6 electrons or V^{-1}. Thus the 24 electron/formula unit compound can be understood as valence balanced composition $V^{-1}Fe_2^{-1}Al^{+3}$.

The full-Heusler structure is very similar to that of half-Heusler compounds with just an additional transition metal atom M' occupying the vacant sub-lattice in the structure. The molecular orbital picture of full-Heusler semiconductor allows for comparison with electronic structure of semiconductor half-Heusler compounds[41]. Similar to half-Heusler compounds, states on either side of the Fermi-level (E_f) in VFe_2Al are formed from transition metal d-states (see Figure 2). In particular, the Γ point states of the first conduction and valence bands show d-orbital character from Fe atoms which constitute the M' sub-lattice. Removing the M' atom from the structure would presumably decrease the number of states close to the E_f and the d-d interaction between transition metal atoms, thereby opening up the band-gap. From this understanding one can explain the larger band-gaps gneerally observed in half-Heusler compounds when compared to full-Heusler compounds such as VFe_2Al and VFe_2Ga. The impact of adding atoms in the M' sub-lattice of the half-

Heusler structure has been studied for TiNiSn. Ni solubility in TiNiSn introduces mid-gap defect states which impact the thermoelectric properties of the material significantly.[9] The main difference between half-Heusler and full-Heusler semiconductors is the electronegativity of the X-atom. While Al is the most electropositive atom in VFe_2Al behaving as a +3 cation, in half-Heusler NbFeSb the Sb atom is the most electronegative and acts as a -3 anion within the Zintl description of the compound.[5]

2.2 Mobility and Effective Mass

The trends in Seebeck coefficient S and electrical conductivity σ for VFe_2Al with temperature and doping are generally that expected from a small band gap semiconductor. With sufficient doping, the electrical properties are determined by one band, either the conduction or valence band. The weighted mobility (μ_w) of charge carriers in the dominant band can be determined from the variation of $|S|$ with σ [48,49] (see Section 4.2). Figure 4a,b shows that μ_w for both electrons and holes is in the range from 250-700 $cm^2V^{-1}s^{-1}$, which is comparable to the best thermoelectric materials, Bi_2Te_3 based alloys[20].

The effective mass (m_s^*), is determined from the dependence of Seebeck on carrier concentration (Figure 4c,d, Section4.2). Since Hall carrier concentration can be affected by magnetic impurities and is often not reported, we used the chemical carrier concentration (n) calculated from the nominal valence electron concentration that includes dopants in the samples.

The conduction band appears to be heavier with values of $m_s^* = 13m_e$ than the valence bands $m_s^* = 5m_e$, where m_e is the mass of an electron (see Figure 4c,d). Such large m_s^* values (density of states effective masses) are typical of half-Heusler compounds[13,23], and
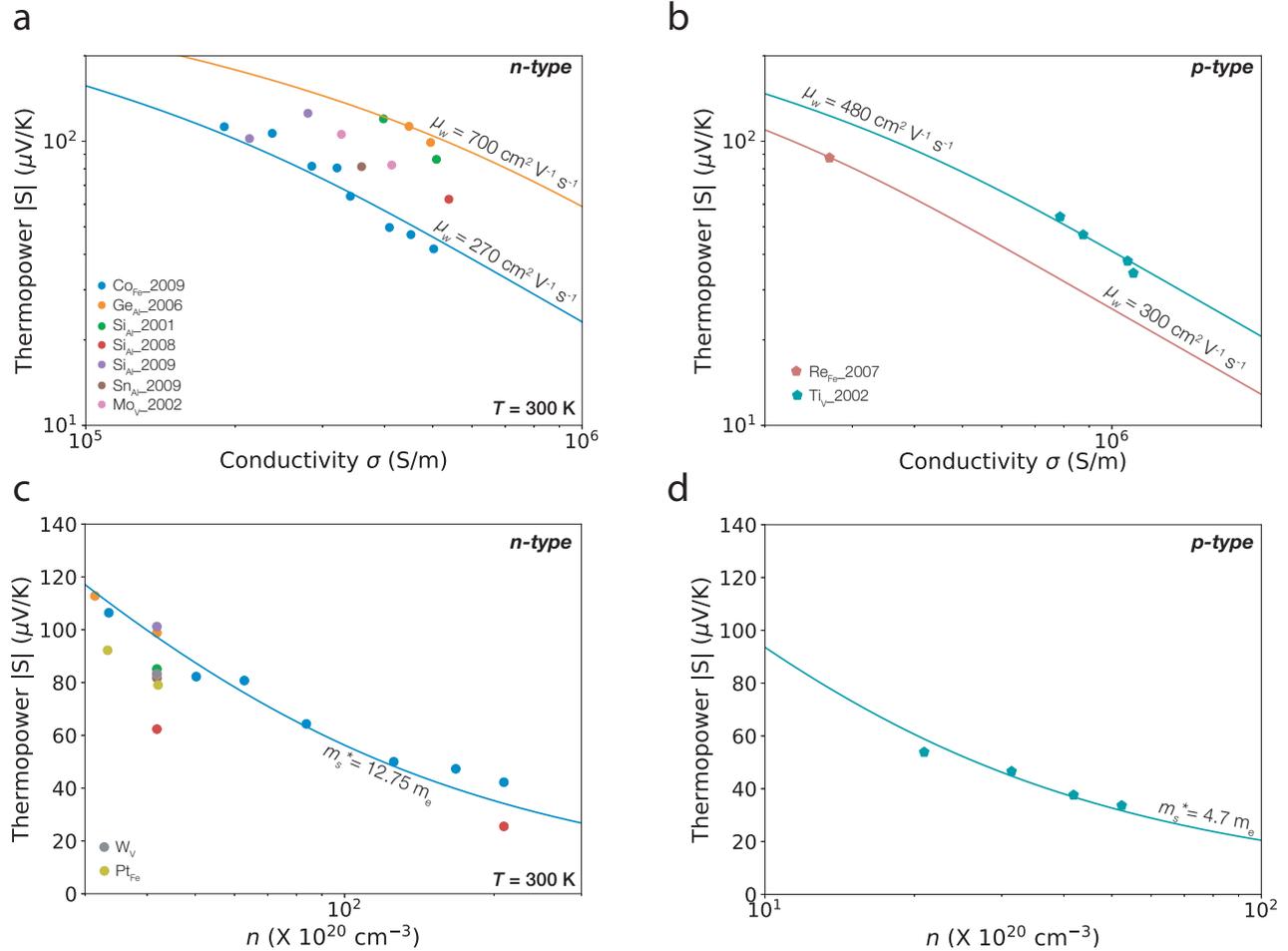
Figure 4 Variation of thermopower ($|S|$) in VFe$_2$Al with different type and concentration of doping[18,19,42–47] at room temperature. (a,b) plot of log$|S|$-log$|\sigma|$ which gives the weighted mobility (μ_w) with n-type (a) and p-type (b) dopants. For both cases, the solid curves represent the prediction corresponding to constant values of μ_w. (c,d) Themopower versus carrier concentration (n) plot to determine the effective mass (m_s^*) of n-type (c) and p-type (d) VFe$_2$Al samples (scatter points). The solid curves show the prediction for a constant m^* which fit reasonably well across the entire range of n.

could indicate multiple band effects particularly at higher carrier concentrations[35].

The reported properties of different dopants in VFe$_2$Al give somewhat different values for μ_w, which could be due to differences in microstructure or changes in the bulk electronic properties. Weighted mobility values are known to be quite sensitive to grain boundaries and interfaces in some materials, such as half Heuslers[50], which can be greatly

altered depending on the synthesis conditions. Typically, samples with larger grain sizes tend to show larger μ_w. We believe that the the the variance in μ_w values of Si samples (400-650 cm^2 V^{-1} s^{-1}) could be explained by such factors.

Changes to the bulk μ_w might be rationalized by considering the atomic contributions to conducting states in the electronic structure. Adding defects to atomic sites that contribute more to the conduction (valence) band are more likely to scatter electrons (holes) and reduce the n-type (p-type) μ_w, as demonstrated in thermoelectric PbSe[51]. For example, the higher μ_w = 480 cm^{2}V^{-1}s^{-1} for Ti doping on the V site when compared to Re-doping on the Fe site (μ_w = 300 cm^{2}V^{-1}s^{-1}, see Figure 4b) is expected because the valence band maximum is dominated by Fe states rather than V states. We further expect p-type samples with substitution on the Al site (e.g. Mg doping) to possibly show even higher μ_w. To the best of our knowledge, this has not yet been investigated. Similarly, a high μ_w for Si and Ge doped VFe$_2$Al is expected because these dopants should substitute on the Al site, which has little contribution to either conduction or valence band. Indeed the μ_w for Si and Ge doped VFe$_2$Al is generally higher than the μ_w for Mo and Co doping (also n-type) where Mo and Co are expected to substitute on the Fe or V site. Mo and Co doping could also change the localized spin state of the transition metals which could lead to spin-disorder scattering of electrons that reduce μ_w[52].

2.3 Band-gap Estimation

The effect on transport properties (electrical resistivity, Seebeck, Hall effect, electronic portion of thermal conductivity, etc.) due to having both electrons and holes (bipolar effect) can be used to estimate the band gap (or negative band gap for a semimetal).
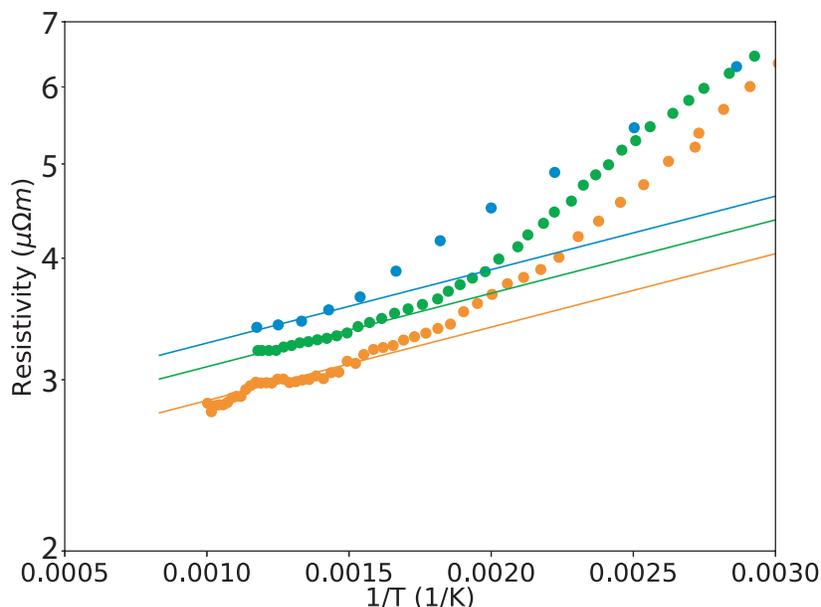
Figure 5 Arrhenius plot for resistivity measurements of three undoped VFe$_2$Al samples (filled circles) from previous reports[19,42,47]. Slope of the solid lines correspond to a small band-gap of E_g=0.03 eV.

Although there is substantial variability in the reported samples and techniques to estimate band gap, the data, using three methods, are generally consistent with a positive band gap in the range of 0.02eV to 0.04eV.

A classic method to estimate band gap of a semiconductor is to examine the temperature dependent resistivity in the intrinsic regime. An Arrhenius plot of the high temperature resistivity data from three, previous reports on undoped VFe$_2$Al samples follows $\rho \propto \exp\left(\frac{Eg}{2kBT}\right)$ suggesting $E_g = 0.03$ eV (see Figure 5). Fitting the data at lower temperatures would give larger values for E_g, possibly explaining the value of 0.1 eV reported in a previous temperature dependent resistivity analysis.[26]

Another common method to estimate band gaps in thermoelectric materials is to use the Goldsmid-Sharp method[53] which examines the peak in thermopower $|S|$ as a function of temperature (Figure 6) in a moderately doped semiconductor using $E_g \approx 2e|S_{max}|T_{max}$.
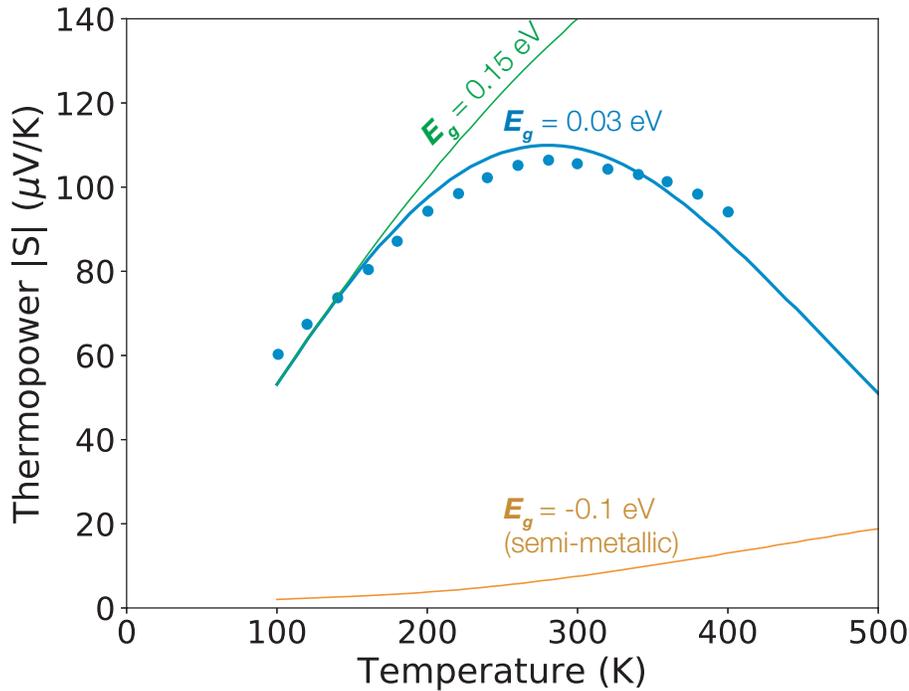
Figure 6 Temperature dependence of Seebeck coefficient for VFe_2Al sample (scatter points) doped with 10% Mo[46]. Solid lines represent predictions from two-band acoustic phonon scattering models with E_g=0.15 eV, 0.02 eV and -0.10 eV (semimetallic). The weighted mobility (μ_w) values used in these models for majority and minority carriers were 440 $cm^2V^{-1}s^{-1}$ and 480 $cm^2V^{-1}s^{-1}$ respectively. Observed temperature dependence of seebeck coefficients for VFe_2Al can be best understood from a small gap semiconductor description of the compound.

For an accurate estimate, the ratio of the weighted mobility of the conduction and valence band is needed[53], which have been estimated from the section above. Once again, we see that a small positive band gap with E_g = 0.03 eV fits much better than a large gap such as E_g = 0.15 eV or negative E_g = -0.1 eV (semimetal, see Figure 6).

The bipolar effect is also noticeable in the low thermopower |S| of lightly doped semi-conductors. For example, the maximum thermopower observed just before or after the transition between p-type and n-type, as a function of doping (Figure 7) also depends on the band gap and weighted mobility ratio. The μ_W and $m_s{}^*$ values attained for electron
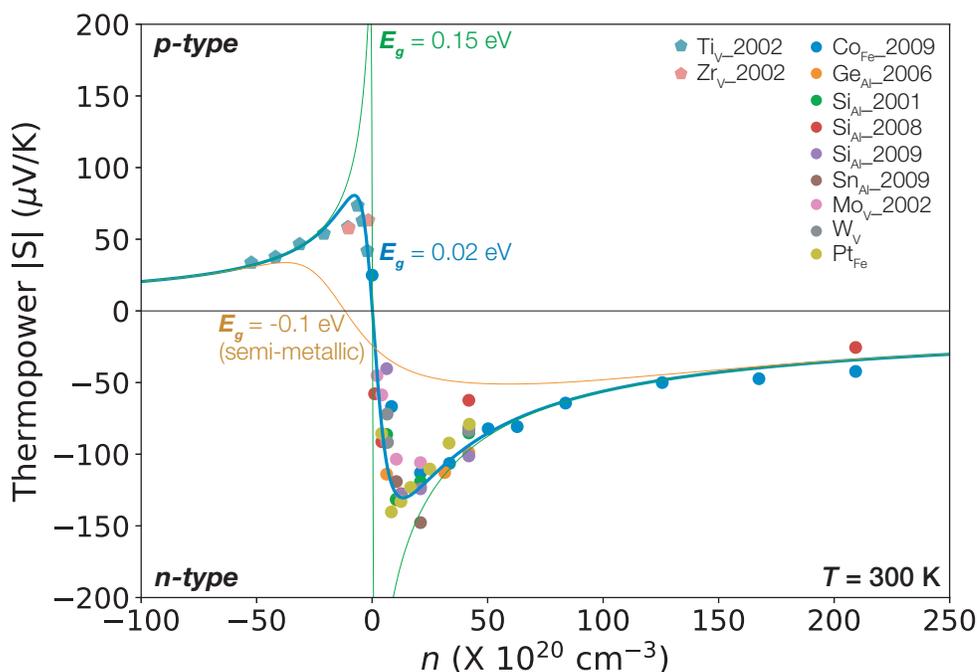
Figure 7 Seebeck versus carrier concentration (n) plot of n- and p-type VFe$_2$Al samples (scatter points) for the entire range of carrier concentration reported in the literature[18,19,42–47]. The solid curves represent two-band acoustic phonon scattering model predictions for band-gap E_g=0.15 eV, 0.02 eV and -0.10 eV (semimetallic). In these models, weighted mobility values of 700 cm^{2}V^{-1}s^{-1} and 300 cm^{2}V^{-1}s^{-1} were chosen for conduction band and valence band transport respectively. Observed seebeck values for VFe$_2$Al can be best understood from a small gap semiconductor description of the compound.

and hole conduction in the previous section can be used to construct a two-band model to predict the Seebeck coefficient at any dopant concentration. The room temperature Seebeck data from a variety of compositions reported in the literature appears to peak around $\sim$ -140 μ V K^{-1} for n-type and $\sim$ +70 μ V K^{-1} for p-type which fits E_g=0.02 eV in the two-band model well (see Figure 7). Increasing E_g above $\sim$0.1 eV gives a very poor fit (see Figure 7). For example, a band-gap of 0.15 eV predicts maximum Seebeck values exceeding 200 $\mu V/K$, which is much larger than any observed value. Similarly, modelling the material as a semimetal with E_g= -0.1 eV predicts Seebeck values smaller than 50 $\mu V/K$

over the entire doping range. The two-band model uses μ_w values of 700 cm^2 V^{-1} s^{-1} for electrons and 300 cm^2 V^{-1} s^{-1} for holes based on the analysis of heavily doped materials above. The large ratio of μ_w values (> 2) leads to the asymmetry in peak Seebeck values observed.

In early experimental reports, VFe$_2$Al has often been described as semimetal based on the observation of a measurable density of states at the Fermi-level.[26] Undoped VFe$_2$Al typically shows a low, metal-like Seebeck coefficient of ≥ 25 $\mu V/K$[18,19,25,42–47,54] and carrier concentrations of the order of $\sim 10^{20}$ cm^{-3}.[24] These findings are actually also consistent with the small gap semiconductor understanding if large intrinsic defect concentrations are considered. Half-Heusler compounds are well-known to accommodate large amounts of intrinsic defects in the cubic structure,[4,5,7–10,55] so a defect concentration of $\sim 10^{20}$ cm^{-3} in VFe$_2$Al is quite plausible especially considering V and Fe have similar chemistry but different number of valence electrons. Using a p-type carrier concentration of 10^{20} cm^{-3}, and the valence band parameters derived above would correspond to a Fermi-level which lies ~ 0.02 eV inside the valence band making the Seebeck coefficient of undoped VFe$_2$Al appear metallic. The small E_g which is consistent with transport properties of the material could also result from presence of defects at elevated temperatures.[56]

2.4   Thermal Modelling

As is often the case for Heusler-type compounds, pure VFe$_2$Al exhibits a large thermal conductivity of about 23 W/m/K, limiting its capability as a thermoelectric. However, point defect scattering of phonons has been shown to drastically reduce the lattice thermal conductivity in numerous studies of VFe$_2$Al with different dopants[18,19,47,57]. Figure 8a

shows the lattice thermal conductivity (κ_L) versus defect site fraction for Si, Ge, and Ta dopants on the Al site[19,58], Re dopant on the Fe site, and Ti dopant on the V site[47]. The lattice thermal conductivity reduction due to point defects trends well with the Klemens alloy scattering model, which includes both the mass and site volume difference on the defect sites (see Section 4.3)[59]. In most cases, there is a non-negligible contribution of the strain scattering due to the volume mismatch at the defect site. The volume difference scaling parameter (ε), which, in theory, should primarily depend on the bonding and elastic properties of the host material, is fit to the experimental data and is between 35-45 for the Si, Ge, and Ta dopant cases, which is well within the expected range for this value[59]. In contrast, the signifcant thermal conductivity reduction due to Re doping can be entirely explained by the large mass difference effect, while the strain scattering is negligible. Finally, Ti doping shows a minute effect on thermal conductivity as a result of its small mass and volume perturbation, and is therefore unattractive as a dopant despite the higher weighted mobility.

Finally, in some reported, sintered samples with sub-micrometer grain size, the lattice thermal conductivity is significantly reduced with undoped samples showing $\kappa_0 \sim$ 15W/m/K[60,61]. Further investigations into microstructural optimization of thermal conductivity are required in this heusler system[62].

We then apply the temperature-dependent model for lattice thermal conductivity discussed in Section 4.3. The umklapp and point-defect scattering effects included in the model appear to capture the measured κ_L versus temperature curves for varying levels of Co dopant (see Figure 8b)[42]. A single, effective Grüneisen parameter value of 2.78 was fit to the data. However, the errors in the calculation of κ_e for a narrow gap semiconductor

a

b
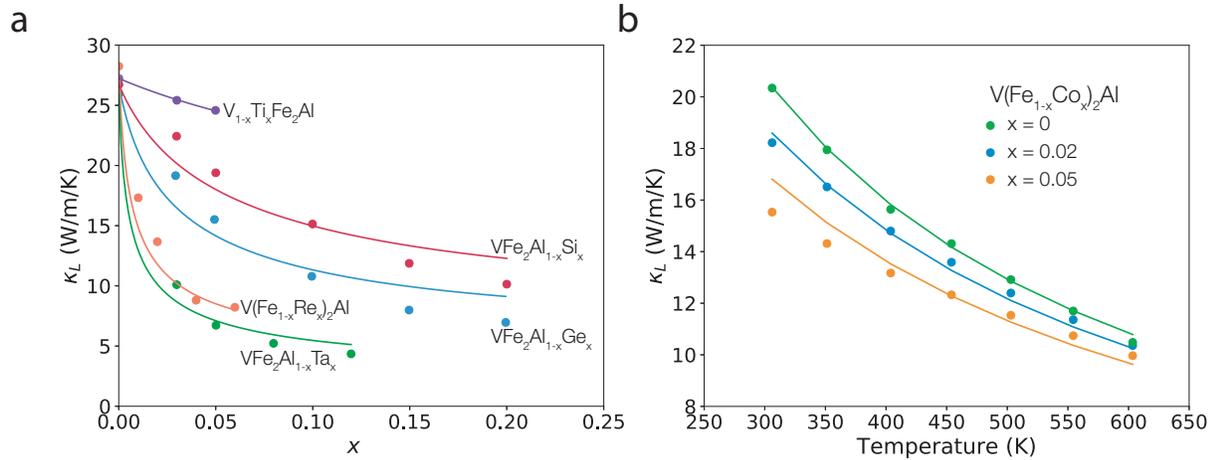
Figure 8 κ_L trends with changes in composition are well described by analytic alloy scattering models. (a) κ_L versus composition curves from the literature[19,47,58] are modelled using the Klemens alloy scattering model. (b) κ_L versus temperature curves with varying Co dopant concentrations from Lu et al.[57] are modelled using point-defect and umklapp scattering theory fit with a single Grüneisen parameter of 2.78.

can affect this value.

By combining this thermal transport modeling with the two-band model for electronic transport, it is then possible to treat the carrier concentration dependence of the thermoelectric figure-of-merit, $zT = S^2\sigma T/\kappa$ (Figure 9). The n-type zT model uses the highest weighted mobility value, $\mu_w = 700 \text{cm}^2/\text{Vs}$, which was found for the Ge_{Al} dopant. Ge doping on the Al site is predicted to be an effective strategy because of its minimal effect on mobility given the lack of Al character seen in electronic states around the Fermi level (see Figure 2). Additionally, Ge_{Al} doping leads to a large thermal conductivity reduction owing to the considerable mass difference effects. On the p-type side, we utilize the weighted mobility and thermal conductivity values for Re_{Fe} doping mainly because of the large thermal conductivity reduction observed for Re doping, again, attributed to the large mass difference at the defect site[47].

The zT versus n trends (see Figure 9) highlight the importance of having a band gap, as

18
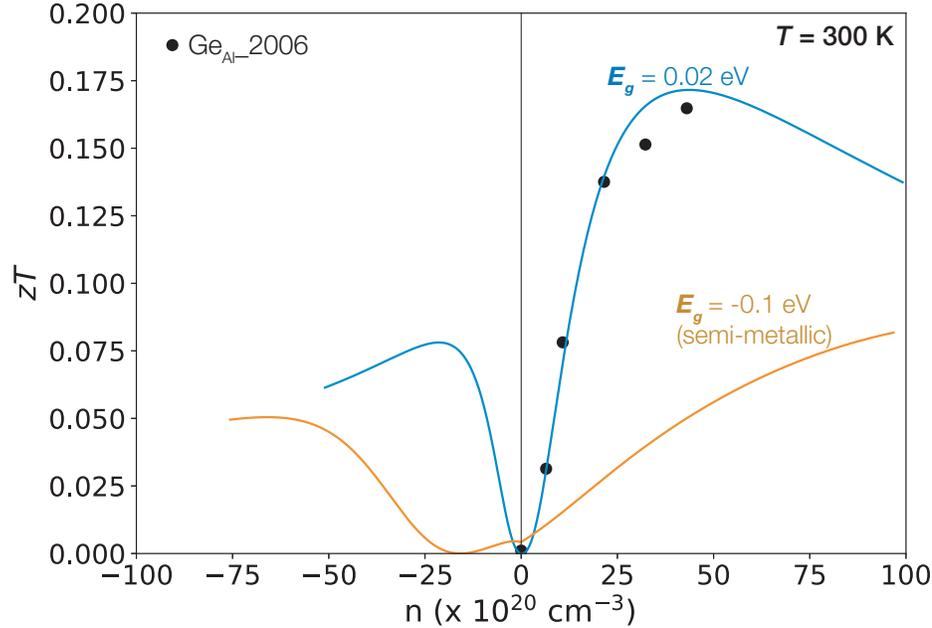
Figure 9 The zT versus carrier concentration (n) curves at 300 K from a two-band model (for $E_g = 0.02$ eV [try 0.03] or -0.1 eV, semi-metallic) emphasize the importance of a band gap to thermoelectric performance. A max zT of 0.17 is predicted for this material at a carrier concentration of 4×10^{21} cm^{-3}. Here, the n-dependence of κ_L is included through alloy scattering using the point defect scattering strength of Ge for n-type and Re for p-type. The zT evaluation from Nishino et al. show good correspondence with the model[19].

the semimetal example shows much lower maximum zT values that occur at very large carrier concentrations. The maximum room-temperature zT values and corresponding carrier concentrations for the true, semiconducting VFe$_2$Al case are listed in Table 1 (ranges express results for a range of E_g values: 0.02-0.04 eV). As suggested by the higher weighted mobility value, the n-type case shows higher thermoelectric performance. This predicted ceiling value on the zT has been experimentally probed in the Ge doping investigation, which doped up to a site fraction of $x = 0.2$[19], and the experimental data lines up well with the two-band model prediction (Figure 9).

Table 1 Summary of parameters used to model the thermoelectric properties of VFe$_2$Al at 300K

	E_g (eV)	μ_{w} (cm^2/V/s)	m^* (m_{e})	Max zT	optimal n, n_{opt}(cm^{-3})	$\kappa_{\mathrm{L}}(n_{\mathrm{opt}})$ (W/m/K)
n-type	0.02	700	12.75	0.17-0.18	4×10^{21}	11.9
p-type	0.02	300	4.7	0.08	2×10^{21}	11.3

3   Conclusion

VFe$_2$Al has drawn considerable attention as a potential inexpensive, environmentally-friendly thermoelectric, because of its large power factor, rivalling commercial n-type Bi$_2$Te$_3$, in both its bulk full-Heusler structure and its metastable, thin film form. With its intermetallic composition and metal-like properties, VFe$_2$Al is historically interpreted as a semimetal, despite its semiconductor-like transport properties common to thermoelectrics. Here, we show that the electronic and thermal transport model as a semiconductor explains experimental data from numerous doping studies. Our two-band electronic transport model shows that the data can only be captured by a narrow-gap semiconductor picture with $E_{\mathrm{g}} \sim 0.03$ eV. The metal-like properties of undoped VFe$_2$Al can be rationalized with a large intrinsic defect concentration of about 10^{20}cm^{-3}.

Our analysis of dopants studied to date, points to Ge$_{\mathrm{Al}}$ and Re$_{\mathrm{Fe}}$ as the most effective n- and p-type dopants, respectively, based on their relative effects on weighted mobility and lattice thermal conductivity. Generally, the band structure and MO diagram analysis performed here points to doping on the Al site as an effective strategy owing to low Al character near the band edge. Finally, the thermal conductivity trends with composition and temperature are shown to be consistent with an analytic treatment of phonon–point-defect and umklapp phonon-phonon scattering. The temperature and carrier-concentration de-

pendence of the zT can be determined by combining the electronic and thermal models, and predicts a maximum room-temperature n-type zT of 0.17 at $n = 4 \times 10^{21} \text{cm}^{-3}$. Increasing the band gap through band structure engineering (e.g. by alloying) will have the most direct benefit to improving zT at or above room temperature. In view of the recent success of VFe$_2$Al as a themoelectric, our findings will be useful for optimally doping both the bulk and thin film thermoelectric materials as well as understanding the fundamental behavior of full-Heusler or metastable VFe$_2$Al.

4 Methods

4.1 Electronic Structure Calculations

First-principles density functional theory (DFT) calculations[63] were performed using Vienna ab initio simulation package (VASP).[64] The Perdew-Burke-Ernzerhof (PBE) exchange correlation functional used in GGA + U.[65] All calculations are performed within the projected augmented wave (PAW) method.[66] Constant U = 0.5 eV and U = 1.35 eV values are used for d-states of both V and Fe atoms respectively in the VFe$_2$Al structure. These values were determined by proportionally scaling down the U values obtained by Do et al.[38] for VFe$_2$Al using constrained DFT calculations (U$_{Fe}$ = 4 eV, U$_V$ = 1.5 eV). Plane-wave basis sets truncated at a constant energy cutoff of 350 eV were used, and Γ-centered k-point meshes with a density of ~27500 k-points per reciprocal atom (KPPRA). All structures were relaxed with respect to cell vectors and its internal degrees of freedom until forces on all atoms were less than 0.1 eV/nm. The density of states calculations were performed using the tetrahedron method on a k-point mesh with mesh density of

$\sim$320000 k-points per reciprocal atom (KPPRA) for both the primitive and supercell calculations. The density of states were evaluated on a grid point density of $\sim$1000 points/ eV. The Electronic structure was plotted using PYMATGEN.[67] The k-resolved Crystal Orbital Hamilton Populations (COHPs) calculations were performed using the version 3.2.0 of the LOBSTER software.[68–70]

4.2 Two-band Model of Electrical Transport

Utilizing experimental datasets from the literature, we parameterize an analytical band transport model to understand the electrical properties of VFe$_2$Al. Evidence of bipolar transport near room temperature and at carrier concentrations less than $\sim 10^{21}$cm^{-3}, suggests the necessity of a two-band model capturing majority and minority carrier transport. Here, we assume carrier lifetime to be limited by acoustic phonon scattering. We first build separate effective mass models for T = 300K transport of the conduction and valence bands, using only samples in the single-band transport regime (entered by nominally doping the compound in excess of $\sim 10^{21}$ cm^{-3} carriers). Therefore, only samples in the regime of linearly increasing $|S|$ response to temperature were chosen

To build the transport models, data was collected from a variety of n-type (Co[42],Si[43–45], Ge[19], Sn[45], Mo[46], Pt[18], W[18]) and p-type (Ti[46], Zr[18], Re[47]) dopants used in previous thermoelectric studies. The weighted mobility— a carrier mobility parameter weighted by the density of states effective mass— is determined from thermopower ($|S|$)-conductivity (σ) relation. The weighted mobility is directly related to the thermoelectric power factor at a given doping level ($\eta = E_{\mathrm{f}}/k_{\mathrm{B}}T$) and temperature. Moreover, the influence of dopants on carrier mobility through effects such as alloy scattering is easy to assess via the weighted

mobility. We also determine the Seebeck effective mass, m_s^*, which relates to the density-of-states at the Fermi level, from the $|S|$ versus carrier concentration (n) relation. These $|S|$-σ-n relations are detailed below through their mutual dependence on doping level η[71]. The Fermi integrals are denoted as: F_j, where j represents the order.

$$\sigma = \frac{8\pi e(2m_e k_B T)^{3/2}}{3h^3}\mu_W F_0$$
$$S = \frac{k_B}{e}\left(\frac{2F_1}{F_0} - \eta\right) \tag{1}$$
$$n = 4\pi\left(\frac{2m_s^* k_B T}{h^2}\right)^{3/2} F_{1/2}$$

Once the fitted band parameters μ_W and m_S^* have been determined for the valence and conduction band, we then build a two-band model in order to fit the band offset (E_g) that best describes the full data (i.e. including samples in the bipolar regime). The two band Seebeck and conductivity equations are shown below combining the electron and hole properties. Here, the relationship $\eta_p = -(E_g/(k_B T) + \eta_n)$ has been fixed when determining σ_p, S_p, and hole carrier concentration p.

$$\sigma = \sigma_p + \sigma_n \qquad\qquad S = \frac{S_p\sigma_p + S_n\sigma_n}{\sigma_p + \sigma_n} \tag{2}$$

4.3 Thermal Transport Models

We use analytical thermal models to understand the carrier-concentration and temperature dependence of the lattice thermal conductivity. It should be noted that the lattice thermal conductivity κ_L is determined by subtracting off the electronic contribu-

tion to the thermal conductivity κ_e, which is difficult to estimate in a narrow gap semi-conductor. Existing two-band models for κ_e can quickly diverge producing anomalously large values as is the case here[71]. Instead, we use the standard Wiedemann-Franz Law $\kappa_e = L\sigma T$ to treat the electronic term, where the Lorentz number L is approximated as $L[10^{-8}W\Omega/K^2] = 1.5 + \exp[-|S|/116\mu V/K]$[72].

We apply the Klemens point defect scattering model to understand the lattice thermal conductivity versus carrier concentration trends. The Klemens model predicts the lattice thermal conductivity ratio of the defective solid (κ_d) to that of the pure solid (κ_0) based on the disorder scaling parameter u:

$$\frac{\kappa_d}{\kappa_0} = \frac{\tan^{-1}u}{u} \qquad\qquad u^2 = \frac{(6\pi^5 V_0^2)^{1/3}}{2k_B v_s}\kappa_0\Gamma. \tag{3}$$

Here, the volume per atom (V_0), lattice thermal conductivity of a reference pure solid (κ_0), and the speed of sound (v_s) are interpolated between end member values[54]. Finally, Γ is the point defect scattering parameter, which is a combination of the mass and site volume difference effects in the defective solids. In both the mass and volume terms, the scattering strength is related to the atomically averaged variance (e.g. $\langle\overline{\Delta M^2}\rangle$) divided by the squared atomic average (e.g. $\langle\overline{M}\rangle^2$). The notation below indicates two levels of averaging in each case, where site averaging on a sublattice is denoted by a bar while the final stoichiometric average of all sublattices is denoted by angular brackets $\langle\rangle$[59].

$$\Gamma = \frac{\langle\overline{\Delta M^2}\rangle}{\langle\overline{M}\rangle^2} + \varepsilon\frac{\langle\overline{\Delta R^2}\rangle}{\langle\overline{R}\rangle^2} \tag{4}$$

The volume difference scaling parameter (ε) is treated as a phenomenological fitting

parameter, but should mainly depend on the bonding and elastic properties of the host material[73].

Additionally, we model the κ_L versus temperature trend by treating scattering due to point defects as well as umklapp phonon-phonon interactions[22]. The relaxation times for each process carry their own phonon frequency dependence and are additionally related to the factors which determine the scattering strength of the interaction. As discussed previously, the scattering strength of a point defect is attributed to the mass and site volume difference at the defect site. Whereas, in the Umklapp scattering case, the scattering strength is determined by the anharmoncity of the lattice as captured by the Grüneisen parameter (γ). Finally, the Debye approximation is invoked, which simplifies the phonon dispersion to $\omega = v_s k$ such that the phonon group and phase velocities are both equal to the speed of sound.

$$\tau_u = \frac{(6\pi^2)^{1/3}}{2} \frac{M_{at} v_s{}^3}{k_B V_{at}{}^{1/3} \gamma^2 \omega^2 T} \qquad \tau_{PD} = \frac{4\pi v_s{}^3}{\Gamma V_{at} \omega^4} \qquad (5)$$

The relaxation times are combined using Matthiessen's rule $\tau_{tot}{}^{-1} = \tau_u{}^{-1} + \tau_{PD}{}^{-1}$ and incorporated in the Callaway-type expression for lattice thermal conductivity. Here, κ_L is defined from a frequency integral up to the Debye frequency ω_D of the spectral heat capacity ($C_s = k_B x^2 e^x / (e^x - 1)^2$ for $x = \frac{\hbar\omega}{k_B T}$), sound velocity, and relaxation time:

$$\kappa_L = \frac{1}{3} \int_0^{\omega_D} C_s(\omega) v_s(\omega)^2 \tau(\omega) d\omega. \qquad (6)$$

5 Conflicts of Interest

There are no conflicts of interest to declare

6 Acknowledgements

Notes and references

[1] Tanja Graf, Claudia Felser, and Stuart SP Parkin. Simple rules for the understanding of heusler compounds. *Progress in Solid State Chemistry*, 39(1):1–50, 2011.

[2] Jun Mao, Zihang Liu, Jiawei Zhou, Hangtian Zhu, Qian Zhang, Gang Chen, and Zhifeng Ren. Advances in thermoelectrics. *Advances in Physics*, 67(2):69–147, 2018.

[3] Jian He and Terry M Tritt. Advances in thermoelectric materials research: Looking back and moving forward. *Science*, 357(6358):eaak9997, 2017.

[4] Wolfgang G Zeier, Shashwat Anand, Lihong Huang, Ran He, Hao Zhang, Zhifeng Ren, Chris Wolverton, and G Jeffrey Snyder. Using the 18-electron rule to understand the nominal 19-electron half-Heusler NbCoSb with Nb vacancies. *Chemistry of Materials*, 29(3):1210–1217, 2017.

[5] Shashwat Anand, Kaiyang Xia, Vinay I Hegde, Umut Aydemir, Vancho Kocevski,

Tiejun Zhu, Chris Wolverton, and G Jeffrey Snyder. A valence balanced rule for discovery of 18-electron half-heuslers with defects. *Energy & Environmental Science*, 11(6):1480–1488, 2018.

[6] Jiawei Zhou, Hangtian Zhu, Te-Huan Liu, Qichen Song, Ran He, Jun Mao, Zihang Liu, Wuyang Ren, Bolin Liao, David J Singh, et al. Large thermoelectric power factor from crystal symmetry-protected non-bonding orbital in half-heuslers. *Nature Communications*, 9(1):1–9, 2018.

[7] Shashwat Anand, Max Wood, Yi Xia, Chris Wolverton, and G Jeffrey Snyder. Double half-heuslers. *Joule*, 3(5):1226–1238, 2019.

[8] Kaiyang Xia, Pengfei Nan, Shihua Tan, Yumei Wang, Binghui Ge, Wenqing Zhang, Shashwat Anand, Xinbing Zhao, G Jeffrey Snyder, and Tiejun Zhu. Short-range order in defective half-heusler thermoelectric crystals. *Energy & Environmental Science*, 12 (5):1568–1574, 2019.

[9] Yinglu Tang, Xiaoshuang Li, Lukas HJ Martin, Eduardo Cuervo Reyes, Toni Ivas, Christian Leinenbach, Shashwat Anand, Matthew Peters, G Jeffrey Snyder, and Corsin Battaglia. Impact of Ni content on the thermoelectric properties of half-heusler tinisn. *Energy & Environmental Science*, 11(2):311–320, 2018.

[10] Shashwat Anand, Kaiyang Xia, Tiejun Zhu, Chris Wolverton, and Gerald Jeffrey Snyder. Temperature Dependent n-Type Self Doping in Nominally 19-Electron Half-Heusler Thermoelectric Materials. *Advanced Energy Materials*, 8(30):1801409, 2018.

[11] S Sakurada and N Shutoh. Effect of Ti substitution on the thermoelectric properties of (Zr, Hf)NiSn half-heusler compounds. *Applied Physics Letters*, 86(8):082105, 2005.

[12] G Rogl, P Sauerschnig, Z Rykavets, VV Romaka, P Heinrich, B Hinterleitner, A Grytsiv, E Bauer, and P Rogl. (V, Nb)-doped half heusler alloys based on {Ti, Zr, Hf}NiSn with high zT. *Acta Materialia*, 131:336–348, 2017.

[13] Chenguang Fu, Shengqiang Bai, Yintu Liu, Yunshan Tang, Lidong Chen, Xinbing Zhao, and Tiejun Zhu. Realizing high figure of merit in heavy-band *p*-type half-heusler thermoelectric materials. *Nature Communications*, 6(1):1–7, 2015.

[14] Hangtian Zhu, Ran He, Jun Mao, Qing Zhu, Chunhua Li, Jifeng Sun, Wuyang Ren, Yumei Wang, Zihang Liu, Zhongjia Tang, et al. Discovery of ZrCoBi based half heuslers with high thermoelectric conversion efficiency. *Nature Communications*, 9 (1):1–9, 2018.

[15] Hangtian Zhu, Jun Mao, Yuwei Li, Jifeng Sun, Yumei Wang, Qing Zhu, Guannan Li, Qichen Song, Jiawei Zhou, Yuhao Fu, et al. Discovery of TaFeSb-based half-heuslers with high thermoelectric performance. *Nature Communications*, 10(1):1–8, 2019.

[16] Guodong Li, Qi An, Umut Aydemir, William A Goddard III, Max Wood, Pengcheng Zhai, Qingjie Zhang, and G Jeffrey Snyder. Enhanced ideal strength of thermoelectric half-heusler TiNiSn by sub-structure engineering. *Journal of Materials Chemistry A*, 4(38):14625–14636, 2016.

[17] MM Al Malki, Q Qiu, T Zhu, GJ Snyder, and DC Dunand. Creep behav-

ior and postcreep thermoelectric performance of the *n*-type half-heusler alloy $Hf_{0.3}Zr_{0.7}NiSn_{0.98}Sb_{0.02}$. *Materials Today Physics*, 9:100134, 2019.

[18] Yoichi Nishino. Development of thermoelectric materials based on Fe_2VAl Heusler compound for energy harvesting applications. *IOP Conference Series: Materials Science and Engineering*, 18:142001, 2011. doi: 10.1088/1757-899X/18/14/142001.

[19] Y Nishino, S Deguchi, and U Mizutani. Thermal and transport properties of the Heusler-type $Fe_2VAl_{1-x}Ge_x$ ($0 \leq x \leq 0.20$) alloys: Effect of doping on lattice thermal conductivity, electrical resistivity, and Seebeck coefficient. *Physical Review B*, 74: 115115, 2006. doi: 10.1103/PhysRevB.74.115115.

[20] Ian T Witting, Thomas C Chasapis, Francesco Ricci, Matthew Peters, Nicholas A Heinz, Geoffroy Hautier, and G Jeffrey Snyder. The thermoelectric properties of Bismuth Telluride. *Advanced Electronic Materials*, 5(6):1800904, 2019.

[21] B Hinterleitner, I Knapp, M Poneder, Yongpeng Shi, H Müller, G Eguchi, C Eisenmenger-Sittner, M Stöger-Pollach, Y Kakefuda, N Kawamoto, et al. Thermoelectric performance of a metastable thin-film heusler alloy. *Nature*, 576(7785): 85–90, 2019.

[22] Eric S Toberer, Alex Zevalkink, and G Jeffrey Snyder. Phonon engineering through crystal chemistry. *Journal of Materials Chemistry*, 21:15843–15852, 2011. doi: 10. 1039/c1jm11754h.

[23] Wolfgang G Zeier, Jennifer Schmitt, Geoffroy Hautier, Umut Aydemir, Zachary M

Gibbs, Claudia Felser, and G Jeffrey Snyder. Engineering half-Heusler thermoelectric materials using Zintl chemistry. *Nature Reviews Materials*, 1(6):1–10, 2016.

[24] Hidekazu Okamura, J Kawahara, Takao Nanba, S Kimura, K Soda, U Mizutani, Yoichi Nishino, M Kato, I Shimoyama, H Miura, et al. Pseudogap formation in the intermetallic compounds $(Fe_{1-x}V_x)_3Al$. *Physical Review Letters*, 84(16):3674, 2000.

[25] Chin-Shan Lue and Y-K Kuo. Thermoelectric properties of the semimetallic Heusler compounds $Fe_{2-x}V_{1+x}M$ (M= Al, Ga). *Physical Review B*, 66(8):085121, 2002.

[26] Yoichi Nishino, M Kato, S Asano, K Soda, M Hayasaki, and U Mizutani. Semiconductorlike behavior of electrical resistivity in heusler-type Fe_2VAl compound. *Physical Review Letters*, 79(10):1909, 1997.

[27] Chin-Shan Lue, Joseph H Ross, et al. Semimetallic behavior in Fe_2VAl: NMR evidence. *Physical Review B*, 58(15):9763, 1998.

[28] DJ Singh and II Mazin. Electronic structure, local moments, and transport in Fe_2VAl. *Physical Review B*, 57(22):14352, 1998.

[29] Ruben Weht and WE Pickett. Excitonic correlations in the intermetallic Fe_2VAl. *Physical Review B*, 58(11):6855, 1998.

[30] GY Guo, GA Botton, and Y Nishino. Electronic structure of possible 3d 'heavy-fermion' compound. *Journal of Physics: Condensed Matter*, 10(8):L119, 1998.

[31] Kiyoshi Ooiwa and Keizo Endo. Nuclear magnetic relaxation in Heusler alloys Fe_2VGa and Fe_2VAl. *Journal of Magnetism and Magnetic Materials*, 177:1443–1444, 1998.

[32] Chin-Shan Lue, Joseph H Ross Jr, CF Chang, and HD Yang. Field-dependent specific heat in Fe_2VAl and the question of possible $3d$ heavy fermion behavior. *Physical Review B*, 60(20):R13941, 1999.

[33] Shivprasad S Shastri and Sudhir K Pandey. A comparative study of different exchange-correlation functionals in understanding structural, electronic and thermoelectric properties of Fe_2VAl and Fe_2TiSn compounds. *Computational Materials Science,* 143:316–324, 2018.

[34] Markus Meinert. Modified Becke-Johnson potential investigation of half-metallic Heusler compounds. *Physical Review B,* 87(4):045103, 2013.

[35] Daniel I Bilc, Geoffroy Hautier, David Waroquiers, Gian-Marco Rignanese, and Philippe Ghosez. Low-dimensional transport and large thermoelectric power factors in bulk semiconductors by band engineering of highly directional electronic states. *Physical Review Letters*, 114(13):136601, 2015.

[36] Shamim Sk, P Devi, Sanjay Singh, and Sudhir K Pandey. Exploring the best scenario for understanding the high temperature thermoelectric behaviour of Fe_2VAl. *Materials Research Express*, 6(2):026302, 2018.

[37] Bin Xu, Xingfu Li, Gongqi Yu, Jing Zhang, Shanshan Ma, Yusheng Wang, and Lin Yi. The structural, elastic and thermoelectric properties of Fe_2VAl at pressures. *Journal of Alloys and Compounds*, 565:22–28, 2013.

[38] Dat Do, Mal-Soon Lee, and Subhendra D Mahanti. Effect of onsite coulomb repulsion

on thermoelectric properties of full-heusler compounds with pseudogaps. *Physical Review B*, 84(12):125104, 2011.

[39] Daniel I Bilc and Philippe Ghosez. Electronic and thermoelectric properties of Fe_2VAl: The role of defects and disorder. *Physical Review B*, 83(20):205204, 2011.

[40] Max Wood, Kazuki Imasato, Shashwat Anand, Jiong Yang, and G Jeffrey Snyder. The Importance of the Mg-Mg Interaction in Mg_3Sb_2-Mg_3Bi_2 Shown Through Cation Site Alloying. *Journal of Materials Chemistry A*, 8:2033–2038, 2020.

[41] Maxwell T Dylla, Alexander Dunn, Shashwat Anand, Anubhav Jain, G Jeffrey Snyder, et al. Machine learning chemical guidelines for engineering electronic structures in half-heusler thermoelectric materials. *Research*, 2020:6375171, 2020.

[42] Wenjia Lu, Wenqing Zhang, and Lidong Chen. Thermoelectric properties of $(Fe_{1-x}Co_x)_2VAl$ Heusler-type compounds. *Journal of Alloys and Compounds*, 484(1-2):812–815, 2009.

[43] Hideaki Kato, Masaaki Kato, Yoichi Nishino, Uichiro Mizutani, and Shigeru Asano. Effect of silicon substitution on thermoelectric properties of Heusler-type Fe_2VAl alloy. *Journal of Japanese Institute of Metals*, 65(7):652–656, 2001.

[44] M Vasundhara, V Srinivas, and VV Rao. Electronic transport in Heusler-type $Fe_2VAl_{1-x}M_x$ alloys (M= B, In, Si). *Physical Review B*, 77(22):224415, 2008.

[45] Eric J Skoug, Chen Zhou, Yanzhong Pei, and Donald T Morelli. High thermoelectric power factor near room temperature in full-heusler alloys. *Journal of Electronic Materials*, 38(7):1221–1223, 2009.

[46] Hitoshi Matsuura, Yoichi Nishino, Uichiro Mizutani, and Shigeru Asano. Doping effects on thermoelectric properties of the pseudogap Fe_2VAl system. *Journal of Japanese Institute of Metals*, 66(7):767–771, 2002.

[47] Fuminori Kobayashi, Naoki Ide, and Yoichi Nishino. Effects of Re Substitution on Thermoelectric Properties of Pseudogap System Fe_2VAl. *Journal of Japanese Institute of Metals*, 71(2):208–212, 2007.

[48] Alex Zevalkink, David M. Smiadak, Jeff L. Blackburn, Andrew J. Ferguson, Michael L. Chabinyc, Olivier Delaire, Jian Wang, Kirill Kovnir, Joshua Martin, Laura T. Schelhas, Taylor D. Sparks, Stephen D. Kang, Maxwell T. Dylla, G. Jeffrey Snyder, Brenden R. Ortiz, and Eric S. Toberer. A practical field guide to thermoelectrics: Fundamentals, synthesis, and characterization. *Applied Physics Reviews*, 5(2):021303, 2018. doi: 10.1063/1.5021094. URL https://doi.org/10.1063/1.5021094.

[49] Stephen Dongmin Kang and G Jeffrey Snyder. Transport property analysis method for thermoelectric materials: material quality factor and the effective mass model. pages 1–5, 2018.

[50] Jimmy Jiahong Kuo, Stephen Dongmin Kang, Kazuki Imasato, Hiromasa Tamaki, Saneyuki Ohno, Tsutomu Kanno, and G Jeffrey Snyder. Grain boundary dominated charge transport in Mg_3Sb_2-based compounds. *Energy & Environmental Science*, 11: 429–434, 2018. doi: 10.1039/c7ee03326e.

[51] Heng Wang, Xianlong Cao, Yoshiki Takagiwa, and G Jeffrey Snyder. Higher mobility

in bulk semiconductors by separating the dopants from the charge-conducting band–a case study of thermoelectric PbSe. *Materials Horizons*, 2(3):323–329, 2015.

[52] Shawna R Brown, Eric S Toberer, Teruyuki Ikeda, Catherine A Cox, Franck Gascoin, Susan M Kauzlarich, and G Jeffrey Snyder. Improved thermoelectric performance in $Yb_{14}Mn_{1-x}Zn_xSb_{11}$ by the reduction of spin-disorder scattering. *Chemistry of Materials*, 20(10):3412–3419, 2008.

[53] Zachary M Gibbs, Hyun-Sik Kim, Heng Wang, and G Jeffrey Snyder. Band gap estimation from temperature dependent Seebeck measurement—Deviations from the $2e|S|_{max}T_{max}$ relation. *Applied Physics Letters*, 106(2):022112, 2015.

[54] C S Lue, Y Kuo, S Horng, S Y Peng, and C Cheng. Structural, thermal, and electronic properties of $Fe_2VSi_{1-x}Al_x$. *Physical Review B*, 71:064202, 2005. doi: 10.1103/PhysRevB.71.064202.

[55] Kaiyang Xia, Yintu Liu, Shashwat Anand, G Jeffrey Snyder, Jiazhan Xin, Junjie Yu, Xinbing Zhao, and Tiejun Zhu. Enhanced Thermoelectric Performance in 18-Electron $Nb_{0.8}CoSb$ Half-Heusler Compound with Intrinsic Nb Vacancies. *Advanced Functional Materials*, 28(9):1705845, 2018.

[56] Alexandre Berche, Martin Talla Noutack, Marie-Liesse Doublet, and Philippe Jund. Unexpected band gap increase in the Fe_2VAl Heusler compound. *Materials Today Physics*, page 100203, 2020.

[57] Wenjia Lu, Wenqing Zhang, and Lidong Chen. Thermoelectric properties of

(Fe$_{1-x}$Co$_x$)$_2$VAl Heusler-type compounds. *Journal of Alloys and Compounds*, 484: 812–815, 2009.

[58] Krystel Renard, Arinori Mori, Yuichiro Yamada, Suguru Tanaka, Hidetoshi Miyazaki, and Yoichi Nishino. Thermoelectric properties of the Heusler-type F e$_2$VTa$_x$Al$_{1-X}$ alloys. *Journal of Applied Physics*, 115:033707, 2014. ISSN 00218979. doi: 10. 1063/1.4861419.

[59] Ramya Gurunathan, Riley Hanus, Maxwell Dylla, Ankita Katre, and G. Jeffrey Snyder. Analytical models of phonon–point-defect scattering. *Phys. Rev. Applied*, 13:034011, Mar 2020. doi: 10.1103/PhysRevApplied.13.034011. URL `https://link.aps.org/doi/10.1103/PhysRevApplied.13.034011`.

[60] M Mikami, S Tanaka, and K Kobayashi. Thermoelectric properties of Sb-doped Heusler Fe$_2$VAl alloy. *Journal of Alloys and Compounds*, 484:444–448, 2009. doi: 10.1016/j.jallcom.2009.04.120.

[61] M. Mikami, Y. Kinemuchi, Y. Ozaki, Y. Terazawa, and T. Takeuchi. Thermoelectric properties of tungsten-substituted Heusler Fe$_2$VAl alloy. *Journal of Applied Physics*, 111:093710, 2012.

[62] M. Mikami, A. Matsumoto, and K. Kobayashi. Synthesis and thermoelectric properties of microstructural Heusler Fe2VAl alloy. *Journal of Alloys and Compounds*, 461:423–426, 2008. ISSN 09258388. doi: 10.1016/j.jallcom.2007.07.004.

[63] Walter Kohn, Axel D Becke, and Robert G Parr. Density functional theory of electronic structure. *The Journal of Physical Chemistry*, 100(31):12974–12980, 1996.

[64] Georg Kresse and Jürgen Furthmüller. Efficient iterative schemes for ab initio total-energy calculations using a plane-wave basis set. *Physical Review B*, 54(16):11169, 1996.

[65] John P Perdew, Kieron Burke, and Matthias Ernzerhof. Generalized gradient approximation made simple. *Physical Review Letters*, 77(18):3865, 1996.

[66] Peter E Blöchl. Projector augmented-wave method. *Physical review B*, 50(24):17953, 1994.

[67] Shyue Ping Ong, William Davidson Richards, Anubhav Jain, Geoffroy Hautier, Michael Kocher, Shreyas Cholia, Dan Gunter, Vincent L. Chevrier, Kristin A. Persson, and Gerbrand Ceder. Python Materials Genomics (pymatgen): A robust, open-source python library for materials analysis. *Computational Materials Science*, 68:314–319, 2013. doi: 10.1016/j.commatsci.2012.10.028. URL `http://linkinghub.elsevier.com/retrieve/pii/S0927025612006295`.

[68] Richard Dronskowski and Peter E Blöchl. Crystal orbital Hamilton populations (COHP): energy-resolved visualization of chemical bonding in solids based on density-functional calculations. *The Journal of Physical Chemistry*, 97(33):8617–8624, 1993.

[69] Volker L Deringer, Andrei L Tchougréeff, and Richard Dronskowski. Crystal orbital Hamilton population (COHP) analysis as projected from plane-wave basis sets. *The Journal of Physical Chemistry A*, 115(21):5461–5466, 2011.

[70] Stefan Maintz, Volker L Deringer, Andrei L Tchougréeff, and Richard Dronskowski.

Analytic projection from plane-wave and PAW wavefunctions and application to chemical-bonding analysis in solids. *Journal of Computational Chemistry*, 34(29): 2557–2567, 2013.

[71] Andrew F. May and G. Jeffrey Snyder. *Introduction to Modeling Thermoelectric Transport at High Temperatures*, pages 1–18. CRC Press, 2012.

[72] Hyun-Sik Kim, Zachary M. Gibbs, Yinglu Tang, Heng Wang, and G. Jeffrey Snyder. Characterization of Lorenz number with Seebeck coefficient measurement. *APL Materials*, 3(4):041506, 2015. doi: 10.1063/1.4908244. URL `https://doi.org/10.1063/1.4908244`.

[73] Heng Wang, Aaron D Lalonde, Yanzhong Pei, and G Jeffery Snyder. The Criteria for Beneficial Disorder in Thermoelectric Solid Solutions. *Advanced Functional Materials*, 23(12):1–11, 2012. doi: 10.1002/adfm.201201576.